Electronic Supplementary Material (ESI) for Physical Chemistry Chemical Physics.

Enhanced electrochemical performance of Li-rich cathode materials through microstructural control

Jon Serrano-Sevillano[a], Marine Reynaud[a], Amaia Saracibar[b], Thomas Altantzis[c], Sara Bals[c], Gustaaf van Tendeloo[c], Montse Casas-Cabanas[a*]

† CIC energiGUNE, Parque Tecnológico de Álava, C/Albert Einstein 48, 01510 Miñano, Álava, Spain

‡ Physical Chemistry Department, Basque Country University, Pharmacy Faculty, Vitoria-Gasteiz, Álava, Spain

§ Electron Microscopy for Materials Research (EMAT), University of Antwerp, 2020, Antwerp, Belgium

Supplementary information

1. Synthesis

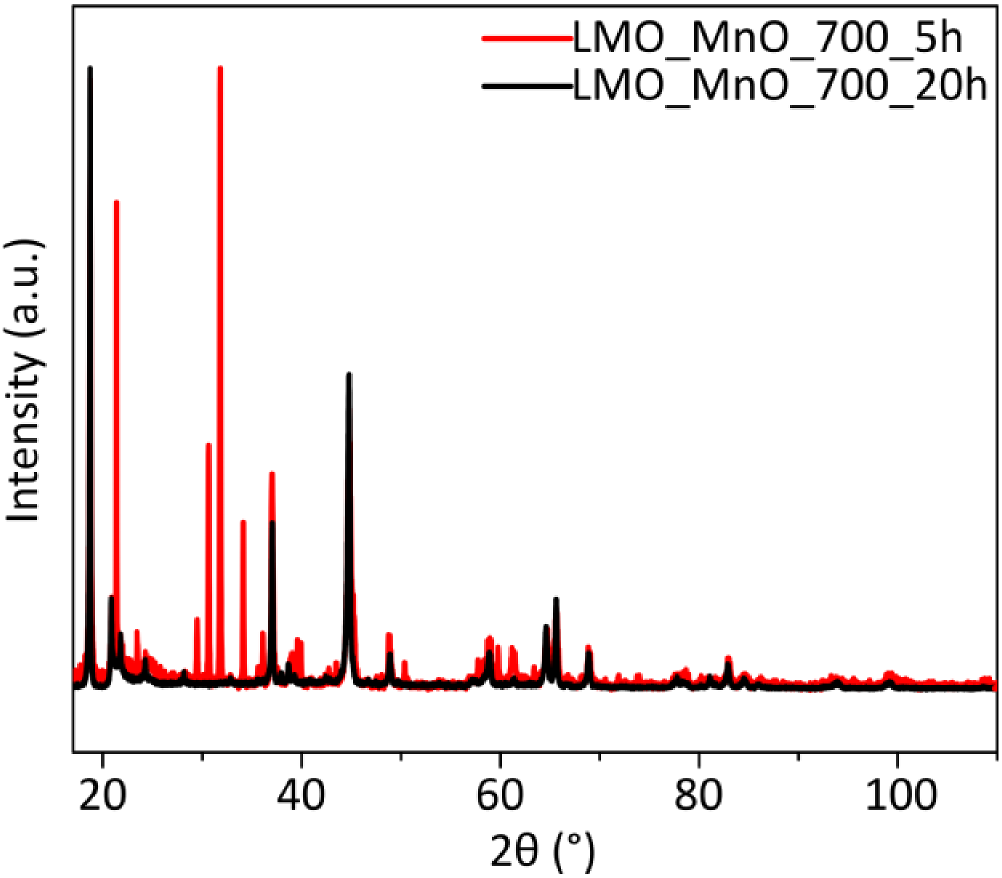

Figure *S*1. Samples synthesized from MnO at 700°C: in black after 5 hours of heat treatment, in red after 20 hours.

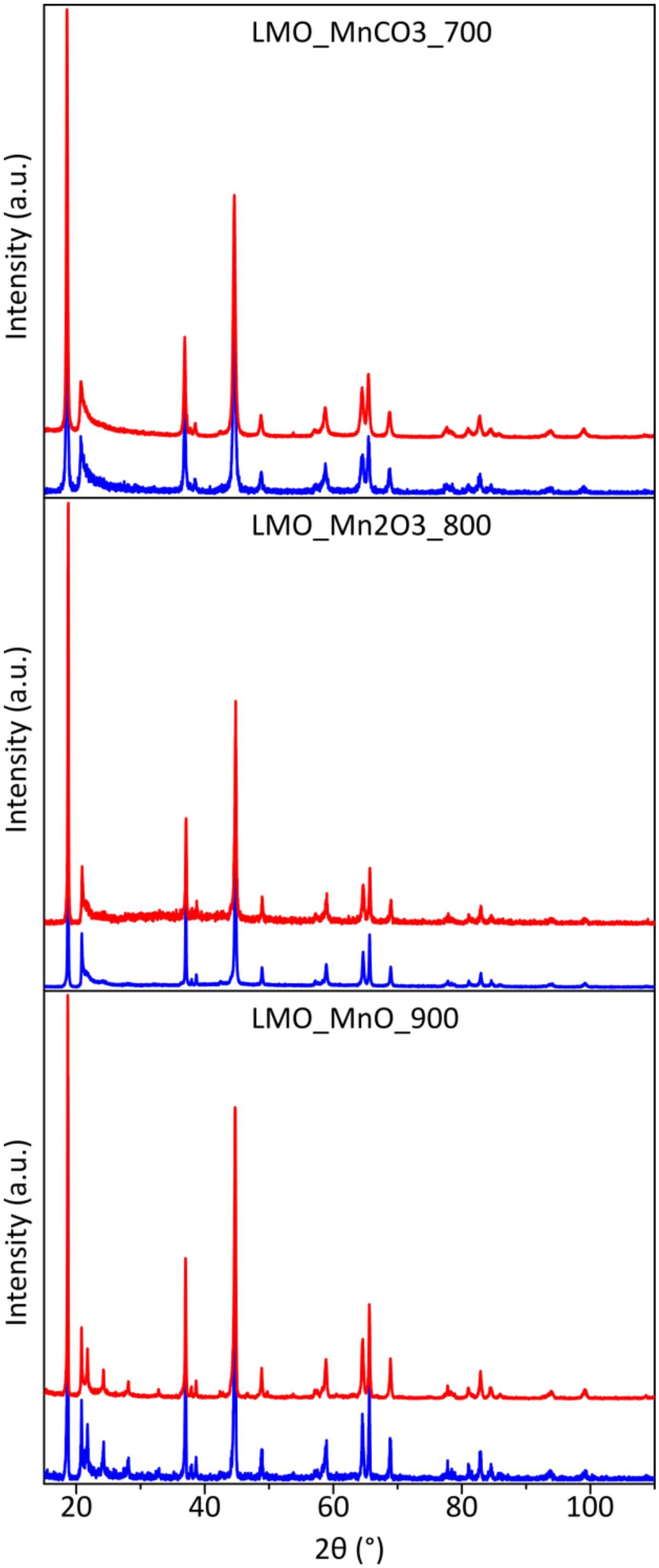

Figure S2. XRD patterns of samples synthesized from different batches in the same conditions.

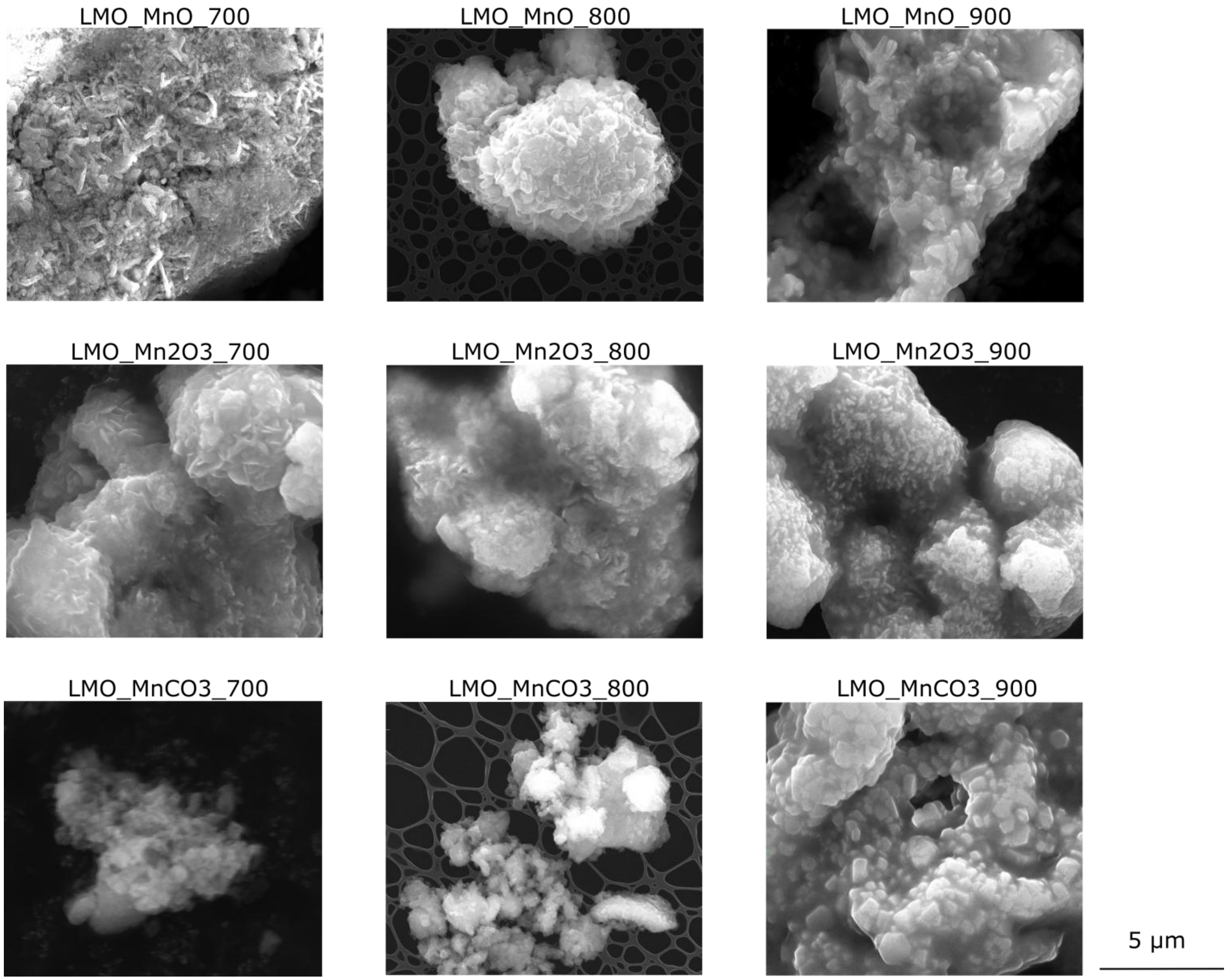

Figure *S*3. SEM images of all synthesized samples.

2. Electron Diffraction

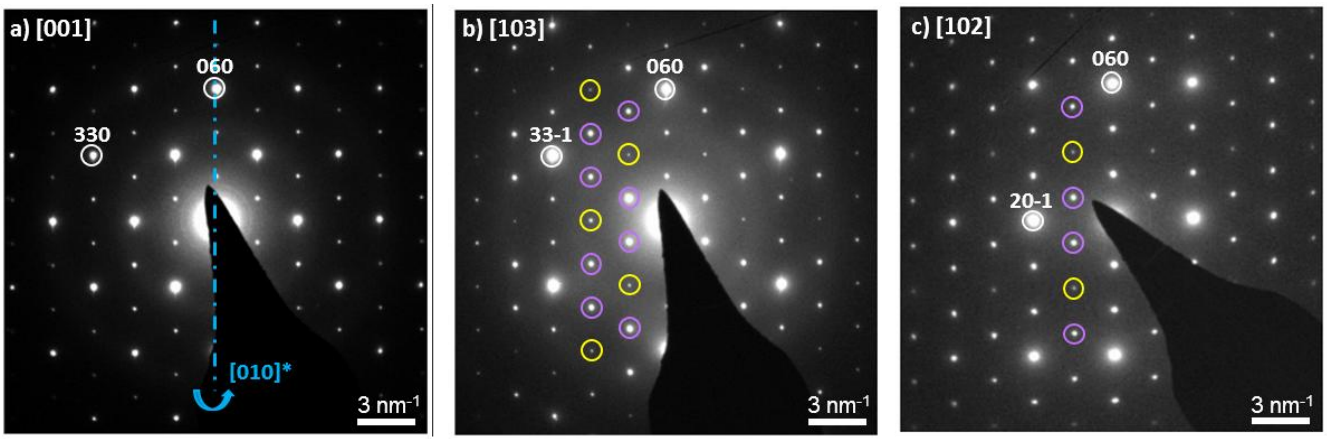

Figure *S*4. SAED patterns obtained from crystals of sample LMO_MnO_900 and indexed according to the (a) [001], (b) [103] and (c) [102] zone axes, showing weak reflections evidencing the honeycomb ordering in the TM layers. The [103] and [102] zone axes are obtained from the [001] one by tilting the sample around the [010]* direction of 19° and 29°, respectively. In (b) and (c), the weak reflections circled in purple and yellow are not explained by the *C*2/*m* unit cell; purple ones result from the interception of diffuse scattering lines observed along the [001]* direction with Ewald's sphere, as shown by Figure *S*6 and previously described by Weill and co-workers [1,2] , while yellow ones result from double diffraction.

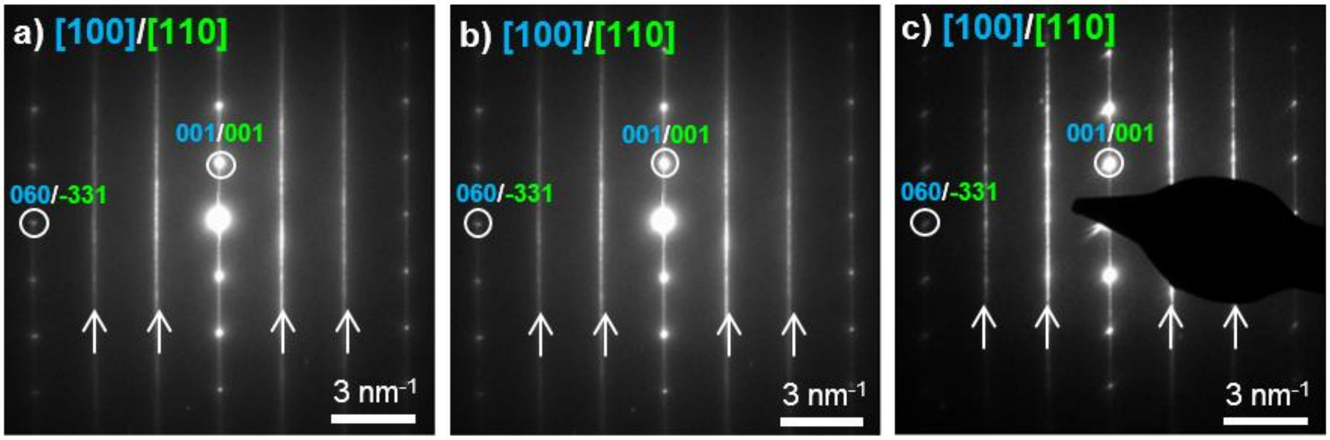

Figure *S*5. Representative SAED patterns from crystals of sample LMO_MnCO3_900, acquired along zone axes perpendicular to the direction of the stacking of the TM layers and indexed according to the $[100]_m$ or $<110>_m$ zone axes.

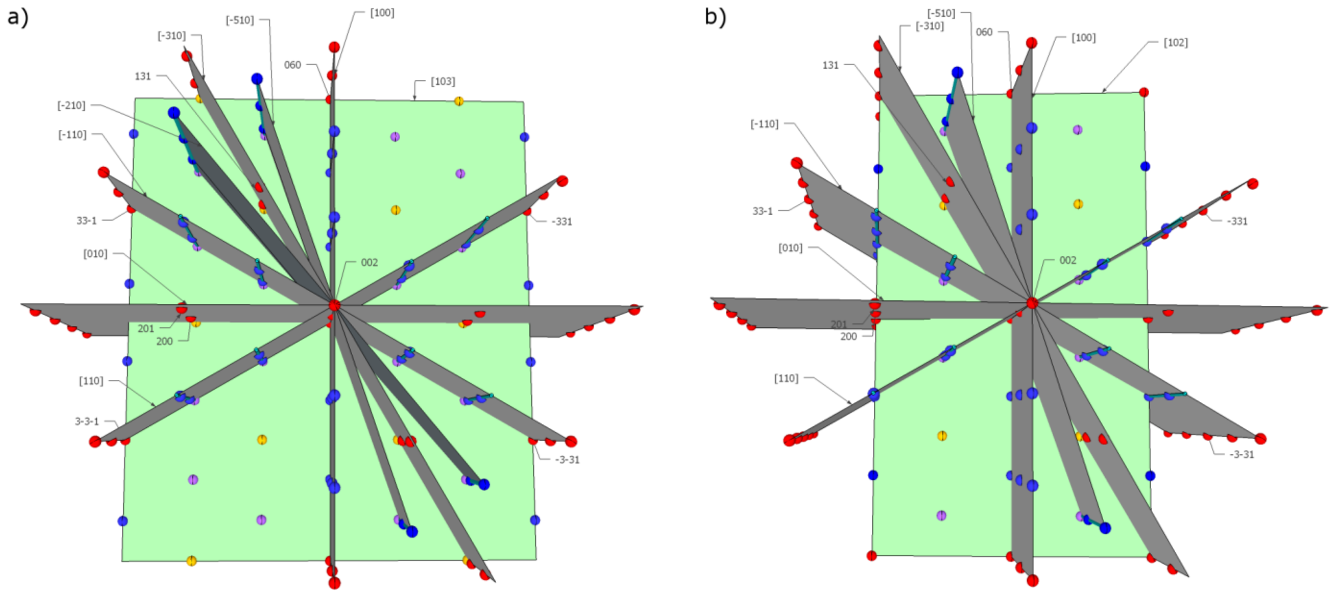

Figure *S*6. 3D representation of the reciprocal space of the *C*2/*m* monoclinic unit cell used to describe Li_2MnO_3 for selected planes. Red spheres indicate the main reflections of the ED patterns; while blue ones indicate the weaker reflections resulting from the Li/Mn honeycomb ordering within the TM slabs. Weak spots observed in the SAED pattern oriented along the [103] zone axis (Figure *S*4) and not explained by the *C*2/*m* unit cell are shown as purple and yellow spheres: purple ones result from the interception of diffuse scattering lines observed along the [001]* direction (represented as blue tubes in the 3D scheme) with Ewald's sphere, as previously described by Weill and co-workers [1,2] , while yellow ones result from double diffraction.

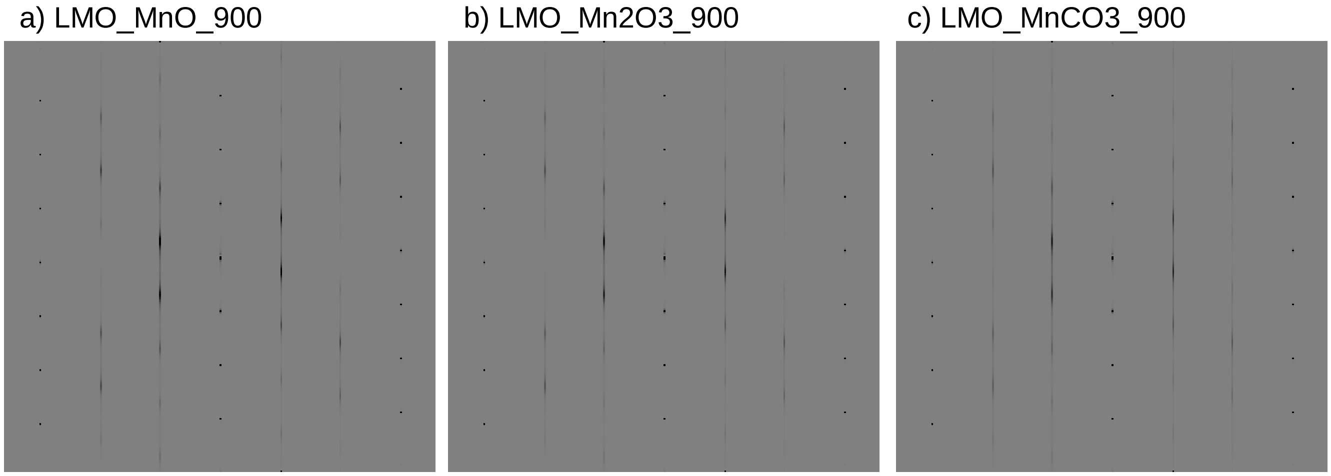
a) LMO_MnO_900

b) LMO_Mn2O3_900

c) LMO_MnCO3_900

Figure S7. Simulations of the ED patterns along the $[110]_m$ direction from the defective structural models refined with FAULTS for samples (a) LMO_MnO_900, (b) LMO_Mn2O3_900 and (c) LMO_MnCO3_900.

3. FAULTS refinements of the XRD patterns

3.1. Structure description of Li_2MnO_3 in FAULTS

FAULTS requires describing the structure as a set of layers that are stacked along a given direction with the help of stacking vectors associated to probabilities of occurrence. These layers have to be defined using a cell which, in order to gain computational time, should be as small as possible. Therefore, to build the FAULTS model, we didn't work with the conventional $C2/m$ unit cell of Li_2MnO_3 but with a smaller one (with P-1 space group), as done in previous works.[3] This triclinic unit cell is obtained from the original $C2/m$ unit cell (Figure *S*8 (a)) with the following transformation: $a_{P\text{-}1} = \frac{1}{2}a_{C2/m} + \frac{1}{2}b_{C2/m}$; $b_{P\text{-}1} = -\frac{1}{2}a_{C2/m} + \frac{1}{2} b_{C2/m}$ and $c_{P\text{-}1} = 1c_{C2/m}$, and an origin shift of ½c. This new P-1 unit cell (Figure *S*8 (b)) has the following cell parameters: $a = b = 4.9265$ Å, $c = 5.0251$ Å, $\alpha = 80.465$, $\beta = 73.099°$ and $\gamma = 60.036°$. Nevertheless, in FAULTS the stacking direction is by definition perpendicular to ab plane, which means that the third axis must be redefined with α and β angles equals to 90° and the norm of this new axis vector set to $c' = 4.7416$ Å (Figure *S*8 (c)). From this FAULTS cell, two types of layers were defined: layer 1 (L1) constituted of the lithium atoms of the Li slabs (lithium layer), and layer 2 (L2) containing lithium, manganese and oxygen atoms (TM layer). Stacking faults were generated using two extra layers in the FAULTS model: layer 3 (L3) and layer 4 (L4) that are equivalent to L2 but that are stacked with different stacking vectors in order to introduce superstructure-type stacking faults (P and P' stacking).

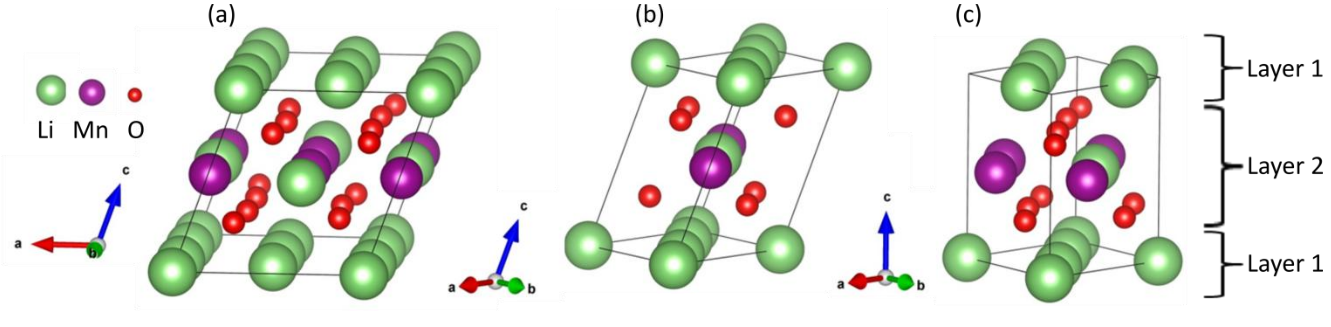

C2/m *P*-1 FAULTS cell

Figure *S*8. Comparison of (a) the *C2/m* unit cell used in conventional Rietveld refinements to describe the non-defective structure of Li_2MnO_3, (b) the smaller equivalent *P*-1 unit cell, and (c) the FAULTS cell used to define the layers to be stacked for the FAULTS refinements.

Table S1 shows the initial structural parameters used for the FAULTS refinements of the XRD patterns of all the samples. As lithium atoms have a low X-ray scattering factor, their atomic positions were not refined. Transition vectors between layers were neither refined, since they are closely correlated to atomic positions. B_{iso} and occupancies were fixed to 1 except for Mn/Li exchange in TM layer; in that case, the sum of Mn and Li occupancies was constrained to 1.

From layer 1, solely transitions to layers 2, 3 and 4 are possible and correspond to R, P and P' stacking, respectively. From layers 2, 3 and 4 there is a unique possible transition to layer 1. The ideal structure is thereby built with a L1 → L2 → L1 stacking sequence.

Table S1. Initial structural parameters used for the FAULTS refinements

a,*b* (Å)	*c* (Å)	γ (°)
4.9265	4.7416	60.036

Layer composition and stacking vectors

Layer	Atom	*x*/*a*	*y*/*b*	*z*/*c*	Occ.	B_{iso}
L1	Li^{I}	0	0	0	1	1
	Li^{I}	1/3	1/3	0	1	1
	Li^{I}	2/3	2/3	0	1	1
L2=L3=L4	Li^{I}	0	0	0	1	1
	Mn^{IV}	1/3	1/3	0	1	1
	Mn^{IV}	2/3	2/3	0	1	1
	O^{II-}	0.3400	0.0000	0.225	1	1
	O^{II-}	0.6500	0.0000	-0.225	1	1
	O^{II-}	0.0000	0.3400	-0.225	1	1
	O^{II-}	0.3400	0.6500	-0.225	1	1
	O^{II-}	0.6500	0.3400	0.225	1	1
	O^{II-}	0.0000	0.6500	0.225	1	1

Possible transition vectors

Transition	*x*/*a*	*y*/*b*	*z*/*c*	Type of stacking
L1 --> L2	1/3	- 1/3	1/2	R
L1 --> L3	2/3	0	1/2	P
L1 --> L4	0	- 2/3	1/2	P'
L2 --> L1	1/3	- 1/3	1/2	R
L3 --> L1	1/3	- 1/3	1/2	R
L4 --> L1	1/3	- 1/3	1/2	R

3.2. Results of the FAULTS refinements for the 9 samples.

Table S2 presents the refined values of the cell parameters obtained from the FAULTS refinement of the XRD patterns of the 9 samples, as well as the degree of defects and apparent crystallite size deduced from the refined values of the stacking probabilities (see section S3.3.) and the peak profile parameters (see section S3.4.), respectively. Table S3 shows the refined atomic positions for the TM layers (L2=L3=L4) for all the samples. Figure S9 (a-f) (together with figure 6 in the main text) show the refined XRD patterns.

Table S2. Refined cell parameters and calculated values of degree of defects and apparent crystallite size, obtained from the FAULTS refinements of the XRD patterns of the 9 samples.

	Temperature (°C)	*a*,*b* (Å)	*c* (Å)	γ (°)	Degree of defects (%)	Size (nm)
LMO_MnO_	900	4.92146(1)	4.73833(4)	60.012(1)	13.2(9)	>500
	800	4.92197(1)	4.73754(5)	60.029(2)	18.9(8)	190
	700	4.92365(1)	4.73819(5)	60.02(2)	20.39(7)	74
LMO_Mn2O3_	900	4.92027(2)	4.74157(4)	60.0186(7)	35.6(4)	247
	800	4.92300(2)	4.73879(4)	60.0317(3)	33.9(2)	193
	700	4.92192(1)	4.73900(4)	60.031(1)	33.3(2)	133
LMO_MnCO3_	900	4.92378(1)	4.73783(3)	60.029(1)	41.6(5)	>500
	800	4.92485(7)	4.73878(3)	60.011(2)	44.2(5)	187
	700	4.92394(3)	4.73631(6)	60.0303(6)	42.1(5)	52

Table S3. Refined atomic positions in the TM layers (L2=L3=L4) obtained from the FAULTS refinements of the XRD patterns of the 9 samples

	LMO_MnCO3_								
	700			**800**			**900**		
Atom	*x*	*y*	*z*	*x*	*y*	*z*	*x*	*y*	*z*
$\mathrm{Li^{I}}$	0	0	0	0	0	0	0	0	0
$\mathrm{Mn^{IV}}$	0.3353(2)	0.3353(2)	0	0.3363(3)	0.3363(3)	0	0.3336(3)	0.3336(3)	0
$\mathrm{Mn^{IV}}$	0.6647(2)	0.6647(2)	0	0.6637(3)	0.6637(3)	0	0.6664(3)	0.6664(3)	0
$\mathrm{O^{II-}}$	0.3579(9)	-0.0057(8)	0.2287(2)	0.37(7)	0.64(7)	-0.22(4)	0.352(3)	0.633(2)	-0.218(1)
$\mathrm{O^{II-}}$	0.64166(4)	0.0064(2)	-0.22842(2)	0.63(8)	0.36(7)	0.22(4)	0.6328(3)	0.3537(2)	0.21792(3)
$\mathrm{O^{II-}}$	-0.0089(3)	0.3727(1)	-0.20930(1)	0.37(4)	0.01(3)	0.20(3)	0.3593(7)	0.0085(8)	0.2200(4)
$\mathrm{O^{II-}}$	0.3581(7)	0.6413(2)	-0.2270(2)	0.63(4)	-0.01(4)	-0.21(3)	0.6290(2)	0.0229(5)	-0.22035(5)
$\mathrm{O^{II-}}$	0.6435(2)	0.36008(5)	0.22715(1)	-0.02(6)	0.36(7)	-0.23(4)	0.00820(8)	0.36123(4)	-0.22024(2)
$\mathrm{O^{II-}}$	0.0083(1)	0.62724(2)	0.2096(8)	0.02(6)	0.64(7)	0.23(4)	0.0289(1)	0.62333(6)	0.21720(6)
	LMO_Mn2O3_								
	700			**800**			**900**		
Atom	*x*	*y*	*z*	*x*	*y*	*z*	*x*	*y*	*z*
$\mathrm{Li^{I}}$	0	0	0	0	0	0	0	0	0
$\mathrm{Mn^{IV}}$	0.33242(5)	0.33242(5)	0	0.33182(5)	0.33182(5)	0	0.3358(2)	0.3358(2)	0
$\mathrm{Mn^{IV}}$	0.66758(5)	0.66758(5)	0	0.66818(5)	0.66818(5)	0	0.6642(2)	0.6642(2)	0
$\mathrm{O^{II-}}$	0.3581(8)	0.6377(3)	-0.2185(2)	0.356(1)	0.6335(7)	-0.2079(3)	0.370(1)	0.6298(1)	-0.2225(2)
$\mathrm{O^{II-}}$	0.6408(1)	0.36016(8)	0.21849(1)	0.62996(6)	0.3551(2)	0.20786(2)	0.62980(6)	0.36949(6)	0.22239(2)
$\mathrm{O^{II-}}$	0.36797(5)	-0.0084(1)	0.23319(4)	0.36477(5)	0.0027(4)	0.22910(3)	0.37539(3)	-0.0018(4)	0.22049(2)
$\mathrm{O^{II-}}$	0.62891(3)	0.0096(1)	-0.23294(1)	0.62384(3)	0.032(2)	-0.2300(9)	-0.221(1)	0.003(3)	0.623(1)
$\mathrm{O^{II-}}$	0.000(1)	0.3640(8)	-0.2271(8)	0.011(1)	0.3579(8)	-0.2280(1)	-0.0033(5)	0.37544(7)	-0.22056(4)
$\mathrm{O^{II-}}$	0.010(1)	0.6333(1)	0.22716(6)	0.0284(2)	0.6275(1)	0.23028(4)	0.0028(3)	0.62368(3)	0.22062(2)
	LMO_MnO_								
	700			**800**			**900**		
Atom	*x*	*y*	*z*	*x*	*y*	*z*	*x*	*y*	*z*
$\mathrm{Li^{I}}$	0	0	0	0	0	0	0	0	0
$\mathrm{Mn^{IV}}$	0,3355(4)	0,3355(4)	0	0,3314(2)	0,3314(2)	0	0,336(2)	0,336(2)	0
$\mathrm{Mn^{IV}}$	0,6645(4)	0,6645(4)	0	0,6686(2)	0,6686(2)	0	0,664(2)	0,664(2)	0
$\mathrm{O^{II-}}$	0.351(2)	0.6472(4)	-0.2026(6)	0.365(3)	0.637(1)	-0.228(1)	0.374(3)	0.631(1)	-0.222(1)
$\mathrm{O^{II-}}$	0.6469(1)	0.35166(6)	0.20238(2)	0.6387(3)	0.3631(2)	0.22731(2)	0.6262(2)	0.3699(2)	0.22176(3)
$\mathrm{O^{II-}}$	0.37406(5)	-0.0186(9)	0.23727(2)	0.3843(5)	-0.025(1)	0.2297(2)	0.379(1)	-0.0054(6)	0.2241(4)
$\mathrm{O^{II-}}$	0.62625(3)	0.0189(3)	-0.23757(2)	0.62418(6)	0.0145(3)	-0.2285(4)	0.62656(9)	0.0037(5)	-0.22120(5)
$\mathrm{O^{II-}}$	-0.01842(9)	0.37394(3)	-0.23771(2)	-0.0250(1)	0.38341(3)	-0.23027(2)	-0.0063(2)	0.38110(5)	-0.22384(3)
$\mathrm{O^{II-}}$	0.0189(1)	0.626(2)	0.237(2)	0.0168(2)	0.62373(4)	0.22787(2)	0.0035(3)	0.62753(4)	0.22109(3)

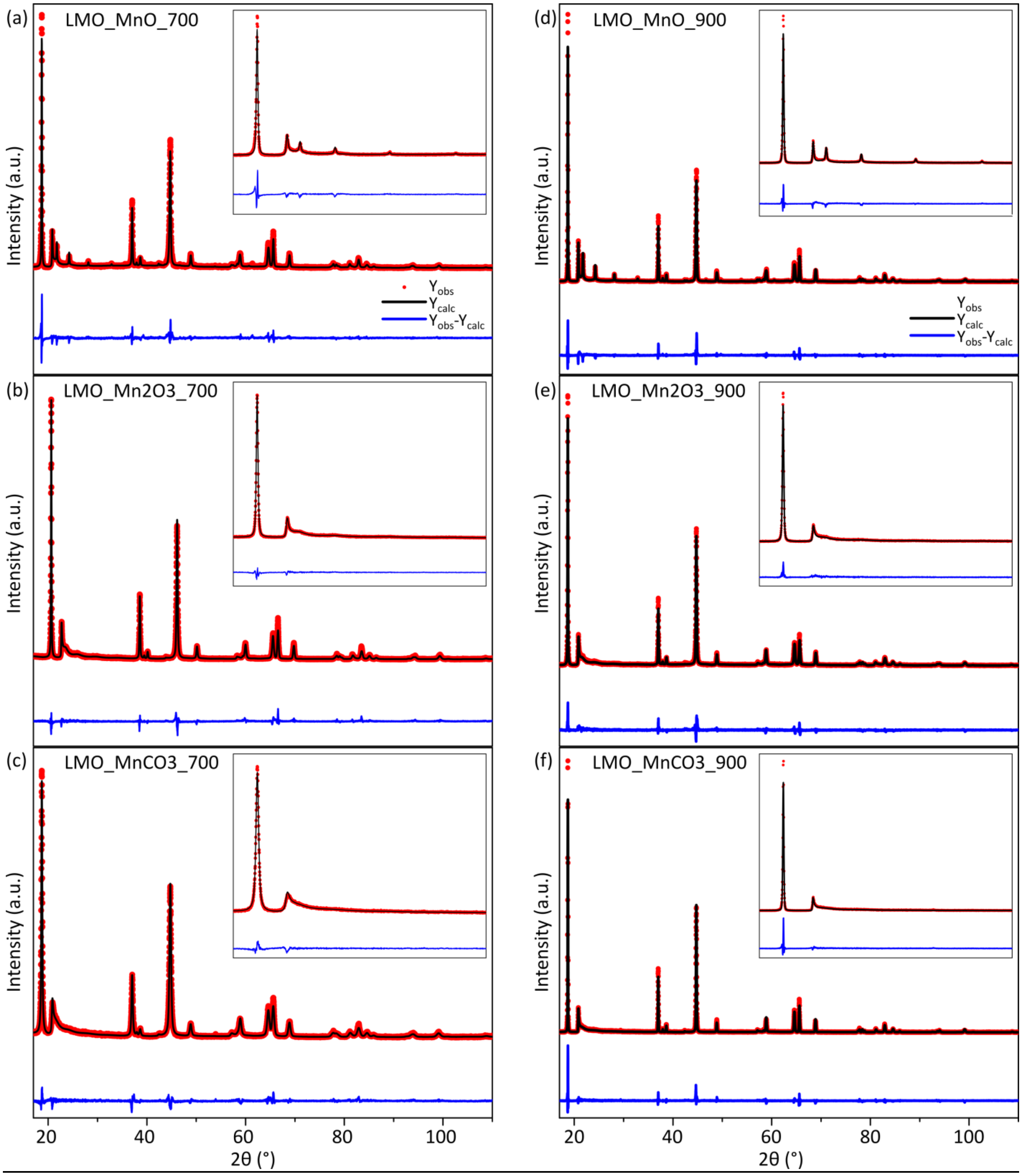

Figure S9. FAULTS refinement of the XRD patterns of (a) LMO_MnO_700, (b) LMO_Mn2O3_700, (c) LMO_MnCO3_700, (d) LMO_MnO_900, (e) LMO_Mn2O3_900, (f) LMO_MnCO3_900. The insets in the figures show the superstructure peaks zone 2θ range 17-35°.

3.3. Calculation of the degree of defect from FAULTS refinements

The ideal stacking consists on a concatenation of L1 → L2 → L1 stacking, being L1 a layer made by pure lithium and L2 a layer made by lithium, manganese and oxygen atoms. A fully disordered sample would be formed by 33% of each of the possible transitions L1 → L2 (= R stacking), L1 → L3 (= P stacking) and L1 → L4 (= P' stacking).

For a more intuitive visualization of the degree of defects, some groups[4,5] proposed a parameter in which the degree of defects was ranked from 0% (100% of ideal stacking and 0% of each stacking fault) to 100% (33% of each stacking possibility). The degree of defects is then obtained from the following formula: $[1-(L_1 \rightarrow L_2)] \cdot \frac{3}{2} \cdot 100$, being $(L_1 \rightarrow L_2)$ the probability for the ideal stacking transition, ranked from 1 (ideal structure) to 1/3 (fully defective structure).

In the case of the refinements treated as two-phase mixtures to describe the particles as a combination of defect-free and defective diffraction domains (i.e. samples synthesized from MnO), the degree of defect of the sample is calculated using the same approach but taking into account the respective weight of each phase in the refinement:

$$\text{Degree of defects} = \frac{[1-(L_1 \rightarrow L_2)] \cdot \frac{3}{2} \cdot 100 \cdot area\ of\ the\ subpattern\ of\ the\ defective\ phase}{area\ of\ the\ subpatterns\ of\ the\ defective\ phase + the\ defect-free\ one}$$

3.4. Calculation of crystallite size from XRD data refinements.

The isotropic apparent crystallite size was calculated from the XRD patterns of the samples using Scherrer's formula (equation 1), where K is equal to 0.89, λ is the wavelength at which the experiment was carried out and H_L is the Lorentzian contribution to the full width at half maximum (FWHM) of the reflection peaks.

$$L = \left(\frac{K\lambda}{H_L}\right)\frac{180}{\Pi} \qquad \text{equation 1}$$

H_L (or FWHM) is calculated from equation 2, as given in the FAULTS manual:[6]

$$H_L = X\tan\theta + \frac{2\lambda}{\Pi D_L \cos\theta}\left(\frac{180}{\Pi}\right) \qquad \text{equation 2}$$

where D_L and X are profile parameters that are adjusted during the FAULTS refinements.
In the refinements, the other profile parameters U, V and W values were set to the instrument resolution function (IRF). The diffractometer was previously calibrated with a corundum sample. H_G, the Gaussian contribution to the FWHM, was treated as infinite ($D_G = 10000$).

4. Stability tests

Figure S10 shows the dependence on time and temperature on defects formation for $MnCO_3$ precursor. The graph shows that until a minimum temperature is reached time has no effect on the ordering of the structure and the degree of defects doesn't vary with the time. At 1000°C, the structure begins to order and if more time is given the order of the structure increases.

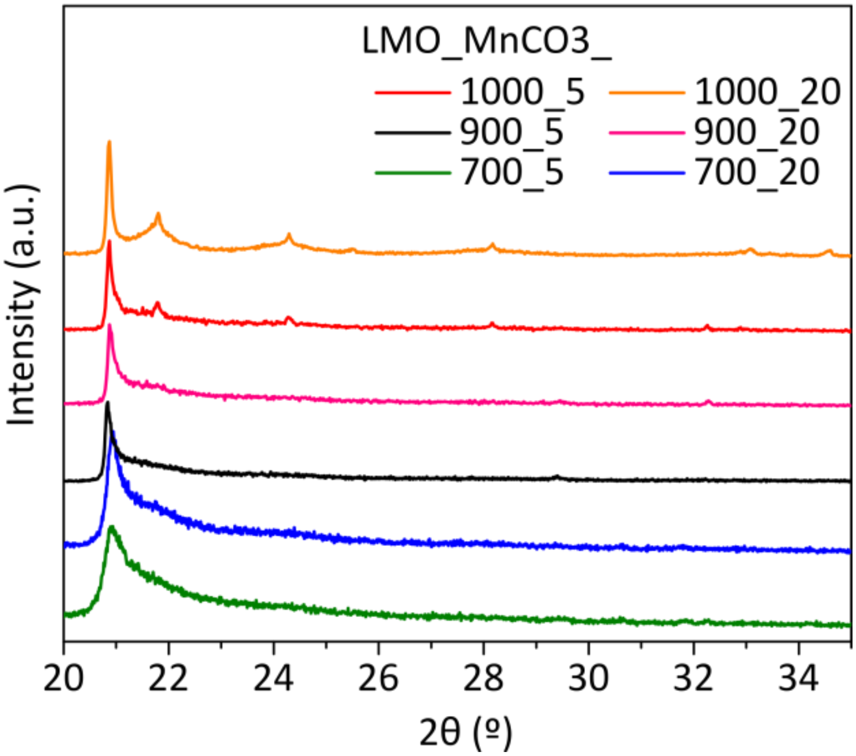

Figure S10. Superstructure region of the XRD patterns of the samples synthesized from $MnCO_3$ precursor at 700°C, 900°C and 1000°C during 5 and 20 hours.

When Li_2CO_3 and Mn_2O_3 are separately heated up to 500°C for 5 hours, they are not altered due to their thermal stability. However, when MnO and $MnCO_3$ are heated, they decompose. Figure S11 (a) shows that MnO partially decomposes in Mn_2O_3, whereas according to Figure S11 (b) $MnCO_3$ decomposes in Mn_5O_8 and Mn_2O_3. If $MnCO_3$ is heated up to 500°C and immediately cooled down (Figure S11 (c)), it does not totally decompose and only Mn_2O_3 is observed as a secondary phase.

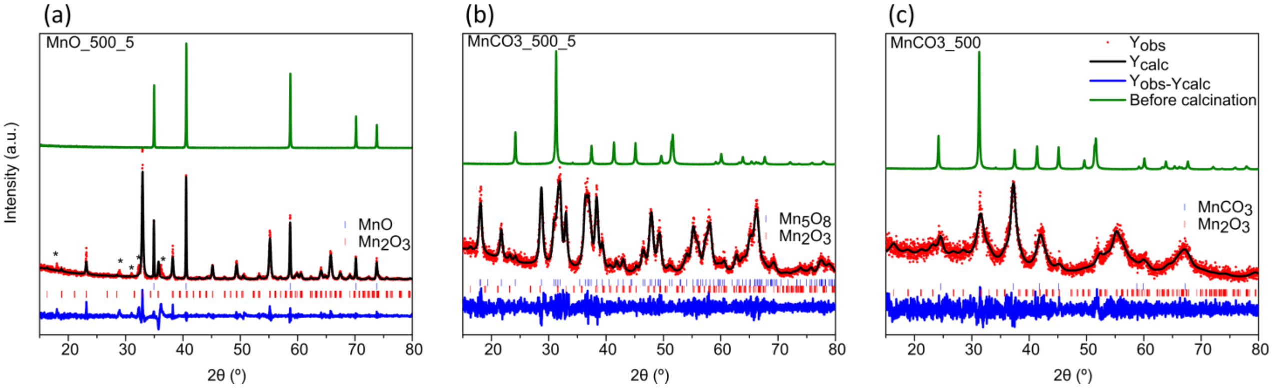

Figure S11. Le Bail refinements of XRD patterns of samples heated at 500°C of (a) MnO for 5 h, (b) $MnCO_3$ for 5 h and (c) $MnCO_3$ for 1 minute. Green curves correspond to the XRD patterns of the phase before calcination.

Figure S12 shows the results of the first calcinations for three samples. Mixtures of Li_2CO_3 and the chosen manganese precursor were heated up to 500°C for 5 h. While in the case of $MnCO_3$ and Mn_2O_3 precursors the main phase is already Li_2MnO_3, for MnO one can observe only a small amount of the targeted phase. This can be explained with the slower kinetics of the MnO-Li_2CO_3 reaction in comparison with the others.

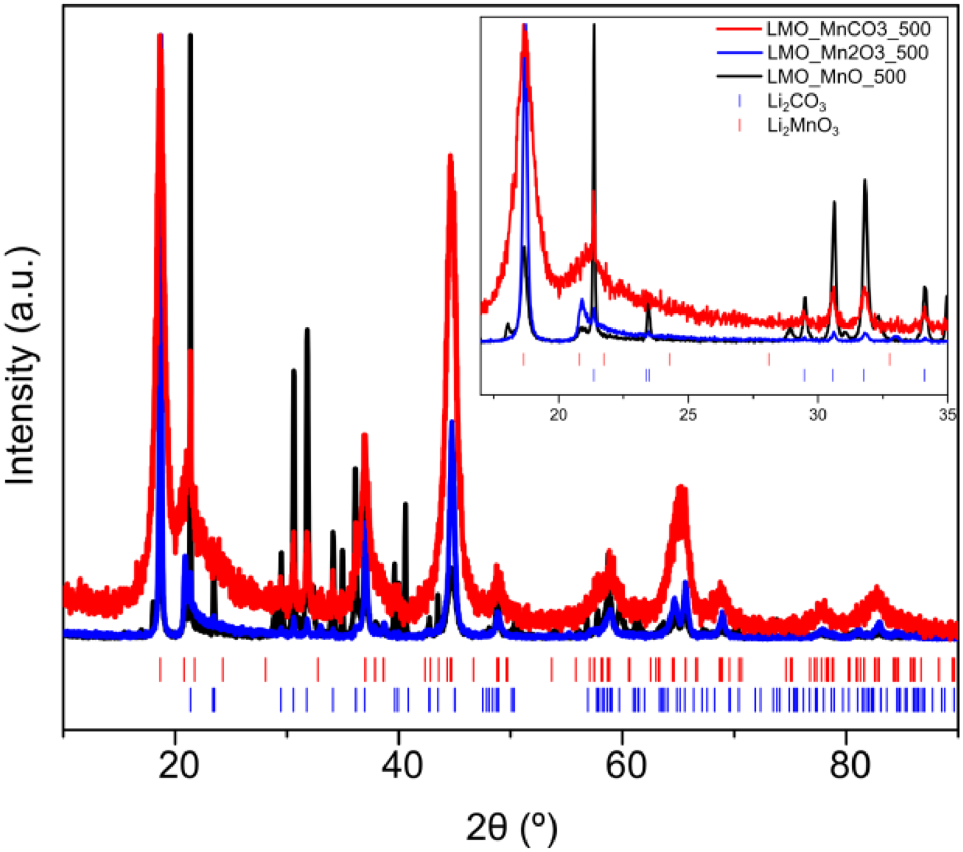

Figure S12. XRD patterns of samples calcinated at 500°C for 5 hours with Li_2CO_3 and a manganese precursor. The main phases present (Li_2MnO_3 and Li_2CO_3) are marked with Bragg's reflections.

5. Electrochemical characterizations

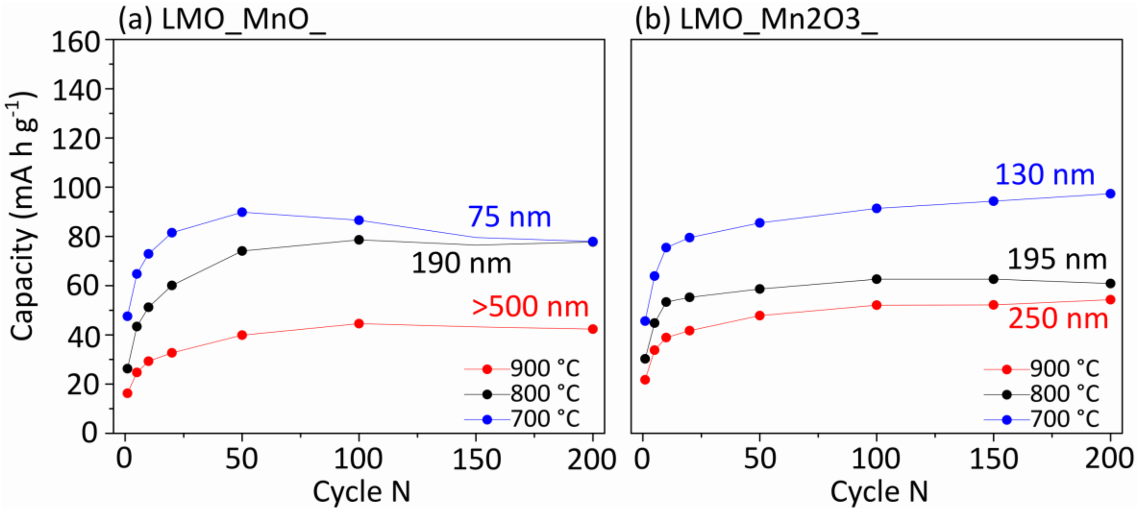

Figure S13. Comparison of the capacity retention obtained for samples synthesized from (a) MnO and (b) Mn_2O_3. Samples synthesized at 900°C, 800°C and 700°C are represented by the red, black and blue lines respectively. For all graphs, results for cycles 1, 5, 10, 20, 50, 100, 150 and 200 are included.

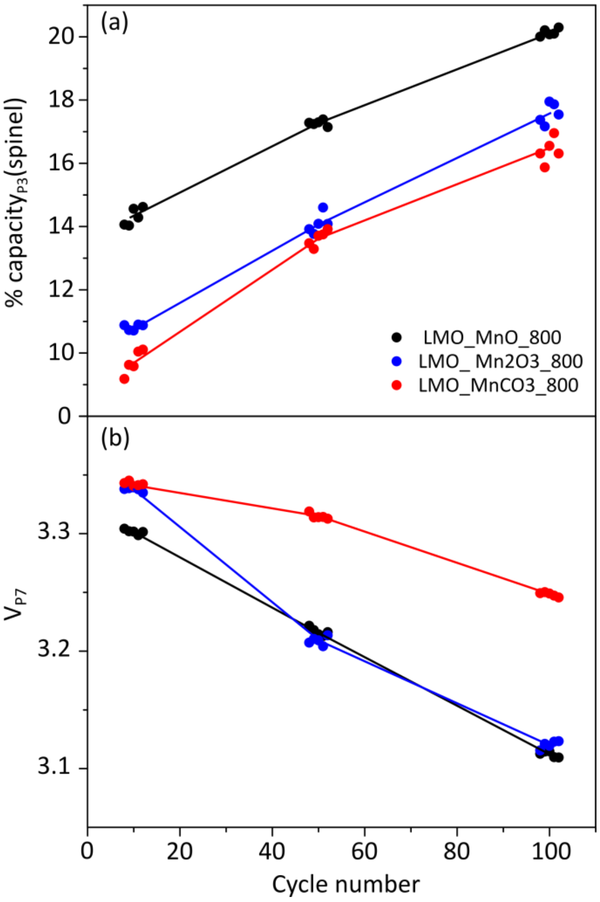

Figure S14. (a) Contribution of the spinel doublet of peaks P3 to the total charge capacity. Cycles number 8-12, 48-52 and 98-102 are shown. (b) Evolution of the average voltage of the reduction peak P7 as function of the number of cycles. For both graphs, dots are the experimental data while the full lines are guides for the eyes.

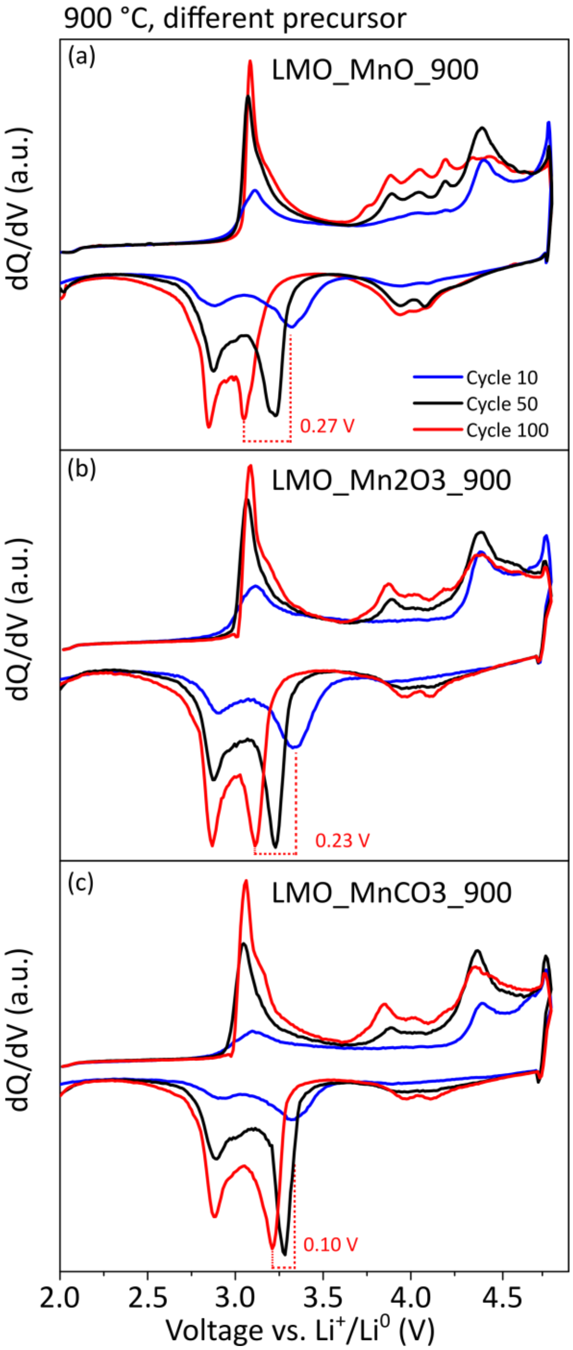

Figure S15. Derivative curves dQ/dV of the 10th, 50th and 100th galvanostatic cycles (blue, black and red lines, respectively) obtained for the samples synthesized at 900°C from (a) MnO, (b) Mn_2O_3 and (c) $MnCO_3$. The voltage drop occurring for the peak at around 3.3 V *vs.* Li^+/Li^0 in discharge between cycles 10 and 100 is highlighted with the red dashed line and the voltage difference is indicated.

References

(1) Boulineau, A.; Croguennec, L.; Delmas, C.; Weill, F. Reinvestigation of Li2MnO3 Structure: Electron Diffraction and High Resolution TEM. *Chem. Mater.* **2009**, *21* (18), 4216–4222.

(2) Weill, F.; Tran, N.; Croguennec, L.; Delmas, C. Cation Ordering in the Layered Li1+x(Ni0.425Mn0.425Co0.15)1 - xO2 Materials (X = 0 and 0.12). *J. Power Sources* **2007**, *172* (2), 893–900.

(3) Casas-Cabanas, M.; Reynaud, M.; Rikarte-Ormazabal, J.; Horbach, P.; Rodríguez-Carvajal, J. FAULTS: A Program for Refinement of Structures with Extended Defects. *J. Appl. Crystallogr.* **2016**, *49* (6), 2259–2269.

(4) Liu, J.; Yin, L.; Wu, L.; Bai, J.; Bak, S. M.; Yu, X.; Zhu, Y.; Yang, X. Q.; Khalifah, P. G. Quantification of Honeycomb Number-Type Stacking Faults: Application to Na3Ni2BiO6 Cathodes for Na-Ion Batteries. *Inorg. Chem.* **2016**, *55* (17), 8478–8492.

(5) Shunmugasundaram, R.; Arumugam, R. S.; Dahn, J. R. A Study of Stacking Faults and Superlattice Ordering in Some Li-Rich Layered Transition Metal Oxide Positive Electrode Materials. *J. Electrochem. Soc.* **2016**, *163* (7), A1394--A1400.

(6) Casas-Cabanas, M.; Rikarte-Ormazabal, J. FAULTS. Available as a Sub-Program of the FullProf Suite at Http://www.ill.eu/sites/fullprof, or as a Separate Program at Http://www.cicenergigune.com/faults. **2015**.